CrystEngComm

Accepted Manuscript

ROYAL SOCIETY OF CHEMISTRY

www.rsc.org/crystengcomm

Manganese sesquioxide to trimanganese tetroxide hierarchical hollow nanostructures: Effect of Gadolinium on structural, thermal, optical and magnetic properties

R. Manigandan[1], K. Giribabu[1], S. Munusamy[1], S. Praveen kumar[1], S. Muthamizh[1], T. Dhanasekaran[1], A. Padmanaban[1], R. Suresh[3], A. Stephen[2] and V. Narayanan[1*]

[1]*Department of Inorganic Chemistry, University of Madras, Guindy Campus, Chennai 600 025.*

[2] *Department of Nuclear Physics, University of Madras, Guindy Campus, Chennai 600 025.*

[3]*SRM University, Bharathi Salai, Ramapuram, Chennai 600089.*

*Corresponding author. Tel: +9144-22202793. E-mail address: vnnara@yahoo.co.in

Abstract

Various hollow manganese oxide (Bixbyite-Mn_2O_3 and Hausmannite-Mn_3O_4) nanoparticles with different morphologies were obtained from the single precursor manganese oxalate (MnC_2O_4). Mn_3O_4 stacked nanostructure instead of coral-like Mn_2O_3 nanospheres were synthesized by thermal decomposition of as synthesized MnC_2O_4 at 700 °C in presence of Gd^{3+} through the oriented arrangement mechanism. The formation process and structural variations by the impact of thermal (450 °C and 700 °C) and cationic dopant Gd^{3+} were analyzed by FTIR, TGA, and XRD. The unexpected size reduction, and significant physicochemical properties were analyzed using various techniques such as, FESEM coupled with EDAX, HR-TEM, DRS-UV-Vis, EPR, EIS and VSM. The addition of gadolinium induces the particle size reduction and phase transition from cubic Mn_2O_3 to tetragonal Mn_3O_4, which leads to the suppression of the electrical conductivity, and changes in the optical band gap. The prepared Mn_3O_4 nanocrystals exhibit ferromagnetic behavior below $T_c \approx 45$ K and weak paramagnetic behavior at room temperature.

Keywords: Bixbyite, Hausmannite, hollow nanostructures, band gap, ferromagnetism

Graphical abstract

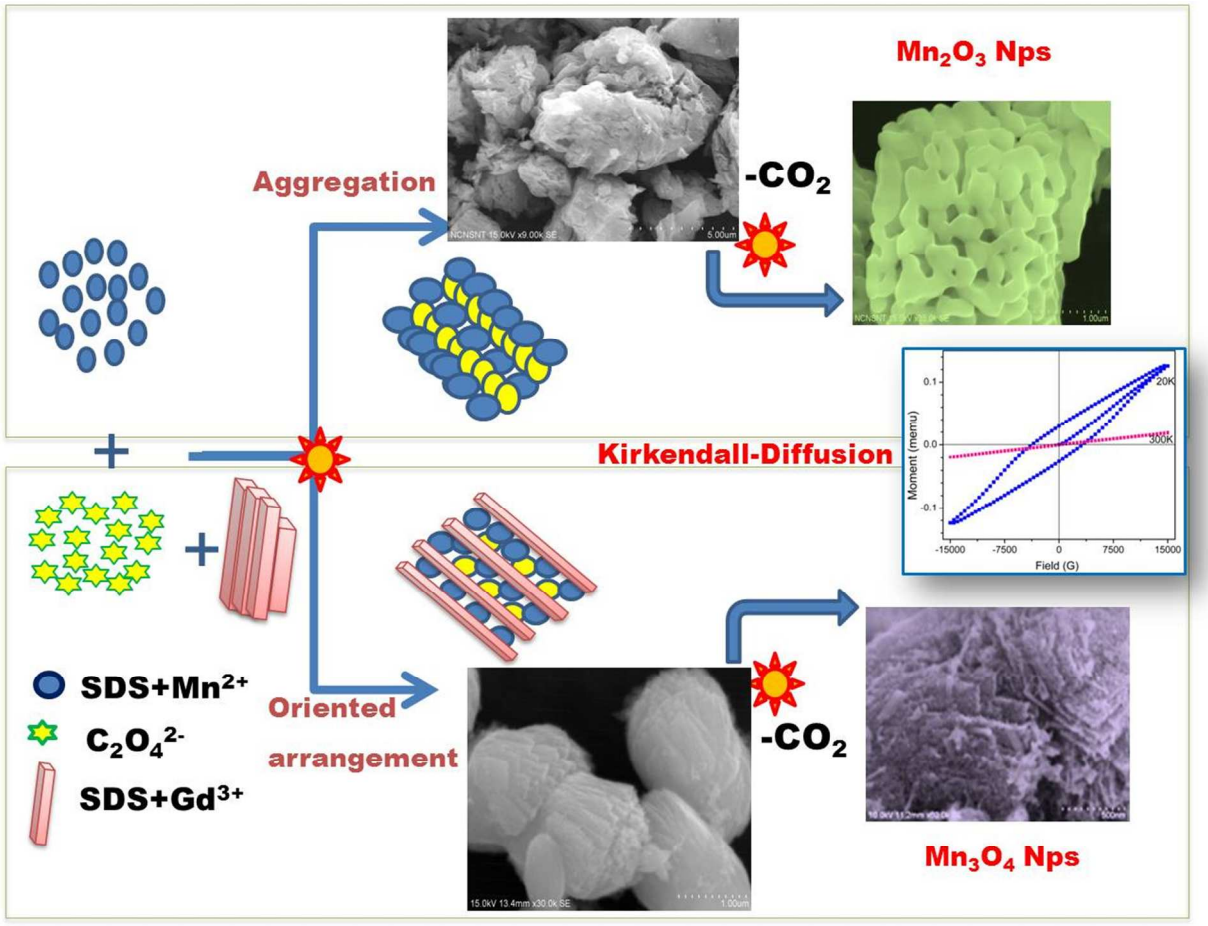

Scheme 1. Schematic representation of the process occurring at different stages which leads to the growth of Mn_2O_3, and Gd-doped Mn_3O_4.

Introduction:

Over the past decades the colloidal magnetic materials with nanoscale have been increased interest in material science, primarily due to the fact that such materials are excellent candidates for technological and scientific application[1, 2]. Nanostructured magnetic metal oxide, manganese oxides and their polymorphs including MnO, MnO_2, Mn_2O_3 and Mn_3O_4 are some of the most attractive materials because of their potential applications in memory devices[3], medical imaging[4], electrode materials in batteries[5], electrochemical sensors[6], catalysis[7], capacitor[8] and in magnetics[9] due to their active magnetic center, fast diffusivities and large surface area. Among them, Mn_2O_3 and Mn_3O_4 have been demonstrated to be one of the low toxicity, inexpensive oxide and earth abundant spinels[10]. The hollow Mn_3O_4 microspheres show good electrochemical performance as anode materials for lithium ion batteries[11].

Most recently, hollow Mn_3O_4 exploiting their room temperature paramagnetism, which have been utilized as positive MRI contrast agents with an enhanced relaxation attributed to an increased water-accessible surface area[12]. The hollow Mn_3O_4 also show a clear antibacterial activity against the Vibrio cholerae, Shigella sp., Salmonella sp., and Escherichia coli bacteria that cause cholera, dysentery, typhoid, and diarrhea diseases, respectively[13]. The Mn_3O_4 microspheres are a good photocatalyst for degradation of methylene blue in presence of hydrogen peroxide[13, 14]. On the other hand, Mn_3O_4 have showed potential applications due to the intimate relationship between unique nanostructures and extraordinary properties[15].

We were aimed to achieve such hybrid metal oxide with nanoscale to improve the physical and chemical properties through creating hollow structure with hierarchical nanostructures by the ion transfer across different solid–solid interfaces in a calcination process. It is necessary to have a general method to prepare hollow NPs with controlled size, cavity and

chemical composition. Thermal decomposition method would be preferred to obtain void structure by the removal of moisture and gaseous impurities. Furthermore, the choice of appropriate metal ion was of primary importance. Among them, Gadolinium, the most abundant element in the rare-earth metal family has tremendous importance, because of its high magnetic moment due to the seven unpaired electrons ($^8S_{7/2}$)[16]. Moreover, gadolinium possesses more unpaired electrons, wide band gap and high ionic radius, which may create a hetero-junction with metal oxide, thus responsible the electrochemical, luminescent and magnetic environment[17-20]. Furthermore, recent studies showed that the doping technique in metal oxide also can efficiently adjust the size, shape and phase of materials[21, 22]. However, to the best of our knowledge, there is no report on influence of Gd ion addition on the morphology, size and phase of Mn_3O_4 nanostructure so far. In particular, the influences of metal ion, especially how they regulate the structural behaviour and morphology of Mn_3O_4 and the appearance of novel optical/magnetic properties, have not been studied thoroughly. Focus of this work, such an understanding is important for optimizing nanostructured material properties by the addition of Gd^{3+} (r = 1.053 Å) due to a large difference in ionic radius[23] and it would be of great interest to gain a better understanding on the origin of physical-chemical properties. Therefore, the variation of the crystal structure upon the cation substitution, as well as dramatic change in the structural, optical, electrical and magnetic properties were investigated. Herein we present the comparatively improved method to synthesize the nanostructured manganese oxide (Bixbyite-Mn_2O_3 and Hausmannite-Mn_3O_4) from the single precursor manganese oxalate. This work mainly pays close attention to the synthesis and characterization of the hybrid manganese oxides, the effect of gadolinium on the phase transition that occurs with the morphology changes from the coral to stacked nanostructures was performed using field-emission scanning electron microscopy

(FESEM), High resolution transmission electron microscopy (HRTEM) determined using X-ray diffraction (XRD). The synthesis of hollow nanostructures is obtained by the mechanism based on the mass transport across the solid–solid interface and Kirkendall effect. The thermal, optical, electrical and magnetic properties of the manganese oxides were demonstrated using TG-DTA-DTG, DRS-UV-Vis, EIS and VSM.

2. Experimental sections

2.1. Materials

Manganese acetate tetrahydrate ($Mn(CH_3COO)_2 \cdot 4H_2O$), Gadolinium nitrate hexahydrate ($Gd(NO_3)_3 \cdot 6H_2O$) was purchased from Sigma-Aldrich. Sodium dodecyl sulfate (SDS), Ammonium oxalate $(NH_4)_2C_2O_4$, and ethanol were purchased from SRL and used as received. Double distilled water used as solvent throughout the experiment.

2.2. Preparation of the Mn_2O_3 and MnC_2O_4:

Manganese oxalate (MnC_2O_4) was prepared by reacting stoichiometric amount of 0.01 M manganese acetate, and 0.025 M ammonium oxalate at room temperature. The 0.24 g manganese acetate and 0.28 g of SDS were dissolved in 90 mL distilled water. After 20 min stirring at 40 °C, 0.177 g of ammonium oxalate in 50 mL of water was added slowly with constant stirring. After few minutes the colorless cloudy precipitate was formed. The resulting precipitate was centrifuged and washed with de-ionized water to remove all the unreacted species. The Mn_2O_3 powder was obtained by decomposing the MnC_2O_4 in air for 2 h at different temperature 450°C, and 700 °C.

2.3. Preparation of the Mn_3O_4 from gadolinium-manganese oxalate:

Gadolinium-manganese oxalate (Gd-MnC_2O_4) was prepared by reacting stoichiometric amount of 0.009 M manganese acetate, 0.001 M gadolinium nitrate and 0.025 M ammonium

oxalate at room temperature. The 0.22 g manganese acetate, 0.045 g of gadolinium nitrate and 0.28 g of SDS were dissolved in 90 mL distilled water. After 20 min stirring at 40 °C, 0.177 g of ammonium oxalate in 50 mL water was added slowly with constant stirring. After few minutes the colorless cloudy precipitate was formed. The resulting precipitate was centrifuged and washed thrice with de-ionized water to remove all the unreacted species from the product. The nano-crystalline Mn_3O_4 was obtained by decomposing the Gd-MnC_2O_4 in air for 2 h at 450 and 700 °C.

2.3 Characterization method:

The crystal structure, grain size and lattice parameter of the sample was determined by Rich Siefert 3000 diffractometer with Cu $K\alpha_1$ radiation (λ = 1.5406 Å). FTIR spectrum was recorded using a Perkin Elmer FTIR spectrophotometer on potassium bromide disks in the range 4000 to 400 cm^{-1}. Electron paramagnetic resonance (EPR) spectrum was carried out with a Bruker EMX 10/2.7 EPR spectrometer (Germany). The morphology of materials was analyzed by HITACHI SU6600 (FE-SEM) FESEM coupled with EDAX and HR-TEM using a FEI TECNAI G2 model T-30 at accelerating voltage of 250 kV. The band gap calculated from the DRS-UV absorbance spectrum was recorded using Perkin Elmer lambda650 spectrophotometer. Thermal analysis was recorded using Perkin-Elmer thermogravimetric analyzer under nitrogen atmosphere. Interpretation of electrochemical impedance spectroscopy (EIS) measurements were analyzed by fitting the experimental impedance spectra to the theoretical model represented by an equivalent electric circuit using AUTOLAB PGSTAT12 (Ecochemie, B.V., The Netherlands) controlled by Frequency Response Analyzer (FRA 4.9) software. The charge transfer resistance (R_{ct}) values were calculated using curve fitting analysis. The peak potential for cyclic voltammogram (CV) was obtained from PGSTAT12 (Eco chemie, B.V., The Netherlands)

Potentiostat/Galvanostat controlled by General Purpose Electrochemical System (GPES 4.9) software. The magnetic properties were measured at room temperature using vibrating sample magnetometer (Lakeshore 7404, USA). The temperature was varied between 20 and 300 K according to a zero-field-cooling/field-cooling (ZFC/FC) procedure at 1000 Oe.

3. Results and discussion

3.1. Phase transformation and structural properties of bixbyte and hausmannite-type manganese oxides:

The crystal structure, crystallite size and lattice parameter of the sample was investigated by XRD. Fig. 1a shows the powder XRD pattern of the MnC_2O_4, undoped and Gd-doped manganese oxides at 450 °C, and 700 °C. Fig 1b corresponds to the pattern of Gd-doped manganese oxides at 450 °C, and 700 °C. The diffraction peaks of MnC_2O_4 was matched to orthorhombic (a=7.143 Å, b=5.870 Å, c=9.021 Å) phase (JCPDS No. 032-0646), with Pmna (53) space group. The diffraction peaks of Bixbyite (450 °C) was assigned to cubic phase (JCPDS No. 078-0390), with Ia-3 (206) space group. The lattice parameters calculated from the XRD pattern for body-centered cubic phase (a=b=c=9.413 Å) and the high intense peak centered at 2θ=33.08°, corresponds to the (222). There were no characteristic changes in the XRD pattern of undoped manganese oxide till 700 °C heating. Furthermore, no crystalline manganese oxide peak can be observed for Gd-doped manganese oxide at 450 °C (Fig. 1b). Upon heating to 700 °C will results the broad diffraction peaks (compared to 450 °C) could be assigned to tetragonal (a=5.770 Å, c=9.435 Å) phase (JCPDS No. 024-0734), with I41/amd (141) space group. The results suggest that the addition of faster-diffusing cationic species (Gadolinium ion) distort the crystal lattice and create the oxygen defect by solid state interface reaction results the formation of spinel structure of Mn_3O_4 instead of Mn_2O_3[24, 25]. In Mn_3O_4 (hausmannite with Mn^{3+} in the

octahedral positions and Mn^{2+} in the tetrahedral positions of the spinel structure) the octahedra were tetragonally distorted due to the Jahn–Teller effect on the Mn^{3+} ion[26]. Moreover, the XRD characteristic peaks were broader, which indicates the smaller crystallite size of Mn_3O_4 compared with the Mn_2O_3. The average crystallite size of the Mn_2O_3 and Mn_3O_4 was calculated from the high intense diffraction peaks based on the Scherrer formula:

$$D_{(hkl)} = K\lambda/\beta Cos\theta \longrightarrow (1)$$

Where, λ = X-ray wavelength, β = full width half maximum (FWHM), D= average crystallite size, θ = diffraction angle, K-shape factor. The calculated average crystallite size was Mn_2O_3 (≈ 67 nm) and Mn_3O_4 (≈ 36 nm). The functional group analysis of the as prepared manganese oxalate and undoped and Gd-doped manganese oxalate calcined at 700 °C were carried out using FT-IR spectroscopy, which was shown in Fig. 2a, b and c, respectively. The spectra revealed the characteristic absorption peaks for metal-oxygen bonding (Mn-O) and oxygen-hydrogen (H-OH) bonding, in Fig. 2a, the spectrum shows that the strong and broad band observed at 1611 cm^{-1}. The bending mode of the O-H groups of coordinated water certainly merged with the carbonyl (C=O) group of the oxalate. The important bands at 1313 with shoulder at 1358 cm^{-1} were related to the stretching vibration of (C-O) of oxalate[27]. The peaks at 524 and 793 cm^{-1} were assigned to vibration of Mn-O and bending vibration of (OCO) coupled with (O-Mn-O) bridge, respectively. Fig. 2b showed the strong bands at about 490 with shoulder at 524 cm^{-1} and strong band at 617 cm^{-1}, which was assigned to the stretching vibration of Mn-O (Mn_2O_3) bond. In Fig. 2c, the peaks around 490, 524, and 590 cm^{-1} were originating from the stretching vibration of the spinel metal oxide ($MnO•Mn_2O_3$). The relative shifts of the peaks which were ascribed to the solid state interaction between gadolinium and spinel manganese oxide. Mn_3O_4 have the normal spinel structure in which the Mn^{2+} ions occupy the tetrahedral

sites while the Mn^{3+} ions occupy the octahedral sites[28].There were no characteristic bands of oxalate and water, which confirms the formation of manganese oxides. The absence of inorganic oxalate, the presence of higher covalent character of metal (Mn^{2+}) facilitated the crystallization of Mn_3O_4 and the absence of secondary phase due to cationic species during higher temperature of calcination were correlated well with the XRD results. EPR spectroscopy monitors paramagnetic species and give details about the oxidation state and coordination of isolated metal site were depicted in Fig.3. The scattering of 'g' values with broad hyperfine structure showed in Fig.3 demonstrates the nanoscale size distribution of crystallites and non-stoichiometry of the system. Consequently, it could be used to characterize the Mn^{2+} and Mn^{4+}, whereas Mn^{3+} species usually cannot be detected due to the complete splitting of energy levels (no ground state degeneracy)[29]. EPR spectra of Mn_3O_4 measured at room temperature shows the broad signal with poorly resolved hyperfine structure. The poor resolved hyperfine curve considerably broadens, which can be explained by the dipole-dipole interactions between magnetic ions in a magnetically concentrated system and shift of the center of resonance may be due to the presence of trace amount second phase Mn_2O_3, which results non homogeneous local magnetic field and modifies the resonance field, and signal shape[30].

3.2. Morphological observation enlightened by FESEM-EDAX and HRTEM

The general morphology of the undoped and Gd-doped manganese oxide samples calcined at different temperature was investigated using FESEM. Fig. 4 shows the FESEM image of a) manganese oxalate obtained at various temperatures at (b) 450, (d) 700, (g) 900 °C, mangnified views are showed with blue arrow line. The close examination of the Mn_2O_3 displays that the surface of the nanostructures contains cracks, small holes and small adsorbed sheets. After calcination up to 700 °C, there were drastic changes in the morphology in both types of

manganese oxides. Thus the morphology of Mn_2O_3 shows coral like architecture with large cavities and surface due to the solid-solid-diffusion. In view of the large volume of CO_2 and coordinated water molecules released out from the metal oxalates with limited dimensional shrinkage during decomposition, there must be a significant void created inside the crystal based on the Kirkendall effect. The similar behaviour was realized for Gd-doped Mn_3O_4 calcined at 700 °C with different morphology. Fig.5 shows the FESEM images of gadolinium doped (a) as obtained oxalate, (b), MnO_x calcined at 450 °C, (c) 450 °C (magnified view) and (d) Mn_3O_4 calcined at 700 °C, respectively. The morphology of Gd-doped Mn_3O_4 was to be slight different when compared to that of undoped Mn_2O_3 at different temperature. The architectures became apparently thread-bundle like nanostructures through the oriented attachment due to the addition of 10 w/w % Gadolinium at 450 °C by the orientation mechanism. Further, stacked nanostructures were achieved from the bundle like nanostructure due to the calcination at 700 °C. Besides this, a certain quantity of nanostructures with smaller size could also be found. The obtained holes on the surface were due to the CO and CO_2 gas evolved at calcination. The HRTEM images of Mn_2O_3 obtained at various temperatures at a) 450, (b) 700, (c) 900 °C were shown in Fig S1. In addition, the elemental analysis was obtained by EDAX analysis shown in Fig. S2. The HRTEM images were shown in Fig. 6(a, b) Mn_2O_3, and (c, d) Gd-doped Mn_3O_4 samples calcined at 450, 700 °C, respectively. HRTEM images reveals that the particles were close to distinct spheres with little aggregation of rod like structure due to the gadolinium ion presence and little agglomeration could be due to the higher temperature, in agreement with the FESEM results. The average diameter of ≈ 152 nm for Mn_2O_3 and ≈ 18 nm (core diameter), ≈ 21 nm (breadth) for Gd-doped Mn_3O_4 (Fig S3) was given in table 1. The crystalline nature of materials analyzed using SAED shown are in Fig.6 (i, ii, iii, iv). This indicates that Mn_2O_3 and

Mn_3O_4 have a consistent crystal structure, Gd doped sample at 450 °C was amorphous in nature, which is in good agreement with the XRD result. The samples calcined at 700 °C (Fig 6 ii, iv) were highly crystalline compared to the SAED pattern obtained for the samples calcined at 450 °C (Fig 6 i, iii). This change in SAED patterns indicates the spontaneous amorphous-to-crystalline transition due to the addition of gadolinium ion along with temperature.

3.3. Formation mechanism:

In general, the obtaining of metal oxides requires a basic medium, and usually alkali hydroxides were involved for this purpose. However, in this work the formation process of Mn_2O_3 and Mn_3O_4 from the manganese oxalate nanocrystals could be explained as follows: firstly, oxalate ions formed as a result of dissociation of ammonium oxalate, which provided a basic condition for nucleation. During the growth process (Scheme-1), the coalescence and growth of the nuclei leads to the formation of three-dimensional crystallites. Therefore, it is fair to think that the medium is basic enough to drive the formation of MnC_2O_4 nuclei the reaction entered the crystal growth stage, which is later decomposed to Mn_2O_3 in presence of atmospheric oxygen with a simultaneous removal of water and large amount of CO_2 molecule may leads to the formation cracks and small pores. Consequently, the manganese oxalate particles formed without large aggregation due to the presence of surfactant. It is worthy to mention herein that, according to the quite different morphological results, the mechanism could be relevant to the oriented arrangement. Further, the morphology of the Gd-doped Mn_3O_4 showed drastic change with respect to Mn_2O_3. Based on the above results, solid-solid-diffusion growth mechanism has been proposed.

3.4. Influence of gadolinium ion on the physiochemical properties:

3.4.1. Optical band gap calculated using DRS-UV-Vis absorbance spectrum

Absorption spectra and band gap energy were measured using DRS UV–Vis spectrometer, in order to characterize the optical properties of the undoped and Gd-doped manganese oxides in the solid state were shown in Fig. 7 a, b, respectively. In the electronic absorption spectrum of the hausmannite and bixbyte type manganese oxide nanoparticles, we were able to recognize few poorly resolved absorption regions. In Fig b, the familiar absorption peak at short wavelength region from 270 to 350 nm was assigned to the spin allowed transition of O^{2-} to divalent (Mn^{2+}) could be merged with the f-f transition (Gd^{3+}) in the ground state $^{8}S_{7/2}$ to the emitting state $^{6}P_{7/2}$ next one from 350 to 490 nm could be assigned to the charge transfer transitions O^{2-} to trivalent (Mn^{3+}). The absorption obtained for both Mn_2O_3 and Mn_3O_4 at visible region up to 800 nm could be reasonably related to d–d crystal field transitions as follows: $^{3}A_{2g}$ $\leftarrow{}^{3}T_{1g}$, $^{3}A_{1g}\leftarrow{}_{3}T^{1g}$, $^{3}T_{2g}\leftarrow{}^{3}T_{1g}$, and $^{3}E_{g}\leftarrow{}^{3}T_{1g}$, on octahedral Mn^{3+} species [31]. The band gap E can be calculated from Eq. (2):

$$(\alpha h\nu) = A(h\nu - E_g)^2 \longrightarrow (2)$$

Where α = is the absorption coefficient, A is a constant, E_g is the band gap and n equals either 1/2 for a direct allowed transition or 2 for an indirect allowed transition. These (direct) band gaps have been deduced from the Tauc plot of $(\alpha h\nu)^2$ vs hν were shown in Fig. 7b. The value of hν extrapolated to α = 0 gives the basic optical band gap energy or direct allowed transition between valence to conduction band excitation of undoped and Gd-doped Manganese oxides were shown in Table 1. The increases in the band gap were due to the particle size reduction of Gd-doped Mn_3O_4. The optical band gap of nanostructures showed blue-shift is reported for the first time with respect to the addition of gadolinium ion at higher temperature due to the quantum confinement effect[32]. According to previous report[20], shift in band gap can be

related to the degree of structural order-disorder in the lattice site by the addition of impurity, which could change the energy levels within band gap of the material.

3.4.2. Thermal behaviour

Fig. 8 shows the TG-DTA-DTG curve of the as prepared Gd-doped MnC_2O_4 and the curve of undoped MnC_2O_4 also given in Fig S4. The TG curves illustrate the weight loss accompanied on Gd-doped MnC_2O_4 by thermal decomposition. The weight loss at till 200 °C was due to the dehydration of the coordinated water molecules and it could be endothermic (inset). The next stages were exhibited due to the decomposition of Gd-doped manganese oxalate to formation of Mn_3O_4 with the throughway of $MnCO_3$ intermediate[33]. It could experience by the process of releasing carbon monoxide and carbon dioxide. Finally, the formation manganese oxide was attained between the temperatures 450-650 °C, which was in good agreement with XRD analysis.

3.4.3. Electrochemical behaviour

EIS measurements were used to evaluate the conducting properties of undoped and Gd-doped manganese oxides. The electrochemical impedance spectra were recorded in the frequency range from 1 MHz to 1 Hz, at the formal potential of the $[Fe(CN)_6]^{3-/4-}$ redox couple. Electrochemical impedance measurements have been conducted on the bare, Mn_2O_3 and Mn_3O_4 as typical Nyquist impedance spectra of the four compounds shown in Fig. 9a, the impedance response of materials exhibits one semicircle in high frequency region, and there is a sloping straight line in the low frequency region. The semicircle is related to the charge transfer through the Mn_2O_3 or Mn_3O_4 covered on the electrode. The numerical value of the diameter of the high frequency semicircle on the Z real axis is approximately equal to the charge transfer resistance. The response at high frequency for bare GCE could be attributed to the counter electrode–

electrolyte interface, while the response at low frequency for samples could be associated with the diffusion processes in the electrolyte[34]. The impedance results show that introduction of gadolinium ion into the manganese oxide supports to raise the intrinsic charge transfer resistance (the intercept of the semi-circle with real axis (Z') at low frequencies is the measure of internal resistance) through the increase in band gap. The electrochemical properties of Mn_2O_3 and Mn_3O_4 will strongly depend on their intrinsic structure. The only differences between undoped and Gd-doped manganese oxides are their crystal structure, as revealed by XRD analysis. Therefore, we can expect that the impedance of the system will be balanced between the Gd ion in the lattice, which increase the resistance and also decrease the electron transfer, indicating that dendritic formation of gadolinium on the surface of spinal structure will lower the diffusion path for the electron[35].

3.4.4. Magnetic property

Fig.10 shows the magnetization as a function of magnetic field (M – H curves) at 300 K, 20 K for Mn_2O_3 (red solid circles) and Gd-doped Mn_3O_4 (blue solid squares) nanoparticles. The magnetization measurements of Mn_2O_3 exhibits typical paramagnetic behavior, but Gd-doped Mn_3O_4 present typical ferromagnetic behavior with large hysteresis at 20 K. While linear behavior in M – H curves indicating the paramagnetic property observed at 300 K. The magnetic materials manifest a well-defined ferromagnetic behavior at low temperature and paramagnetic behavior at room temperature, which was due to the higher thermal energy than the anisotropy energy of the particles[36, 37]. It is known that the physical properties of materials were closely related to their structures and morphologies. In this respect, nanomaterials exhibit them more obviously than bulk materials. Obviously, the values of magnetization in Mn_3O_4 materials were smaller than that of Mn_2O_3 (Fig. 10a), which could be attributed to the smaller particle size

(increase of surface to volume ratio). The coercivity values (H_c) of Mn_3O_4 at 20 K was 3544 Oe. The greatly enhanced coercivity in Mn_3O_4 could be attributed to the effect of isolation of Mn_3O_4 particles by dendritic formation of gadolinium particles, which reduced the magnetic interaction between the Mn_3O_4 particles[38]. The temperature dependence of the magnetization curves, M/T, for the field-cooled (FC) and zero-field-cooled (ZFC) Mn_3O_4 nanostructures under an applied magnetic field of 1000 Oe between 20 and 300 K were shown in Figure 11. From ZFC curve (open circles), an obvious transition from paramagnetic to ferromagnetic behavior can be observed with temperature decrease, FC/ZFC curves are split below the blocking temperatures $T_B \approx 41$ K (lower than Curie temperature, $T_C \approx 45$ K), and the ZFC data shows a maximum at 35 K. This work emphasizes the essential to use these Mn_3O_4 with room temperature paramagnetic and low temperature ferromagnetic properties and tailorable nanostructures were promising for sensing platform as well as biological performance.

4. Conclusion:

In summary, we have succeeded in the synthesis of bixbyte type nanocorals and hausmannite type nanostructures with uniform size by a simple thermal decomposition of manganese oxalate precursor. Hierarchical hollow nanostructures with interior void spaces were attractive candidates owing to the various applications. Hybrid hollow structures facilitates electron transport across the both sites at this hetero-junction results new and improved properties like structural, morphological, electrical, optical, and magnetic properties. The addition of gadolinium induces a cubic Mn_2O_3 to tetragonal Mn_3O_4 phase structural transition, which leads to the increase of the charge transfer resistance, optical band gap, and ferromagnetic properties. Mn_3O_4 prepared by current method and further functionalization are indispensible and responsible for the optical, sensing and biomedical application.

Acknowledgement

The authors acknowledge National Centre for Nanoscience and Nanotechnology, University of Madras, for providing financial support and FE-SEM, DRS-UV-Vis and HRTEM facilities.

Table 1:

Calcined at 700 °C	XRD				HRTEM Size (nm)	UV-VIS Bandgap Eg (eV)	EIS ohm	VSM Coercivity Oe
	2θ°	$d_{(hkl)}$(Å)	FWHM °	Lattice parameters				
Mn_2O_3 (Bixbyite)	32.96	$2.71_{(222)}$	0.215± 0.017	a = 9.413	≈ 152 (diameter)	1.23	573	-
Gd-Mn_3O_4 (Hausmannite)	36.06	$2.48_{(211)}$	0.386± 0.091	a=5.770 b=9.435	≈18(diameter) ≈21(breadth)	1.53	1450	3544(20K) $T_C \approx 45$ K

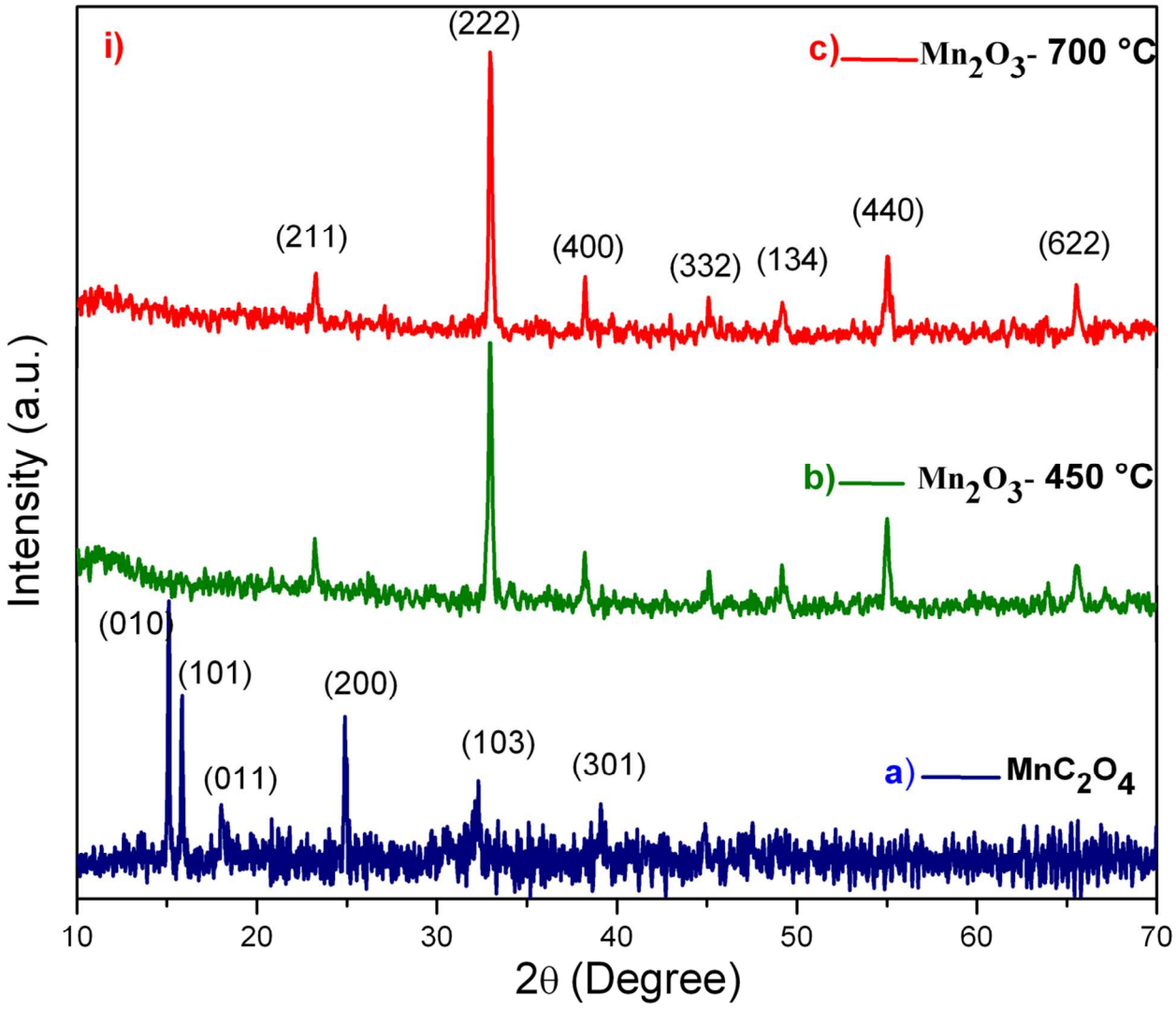

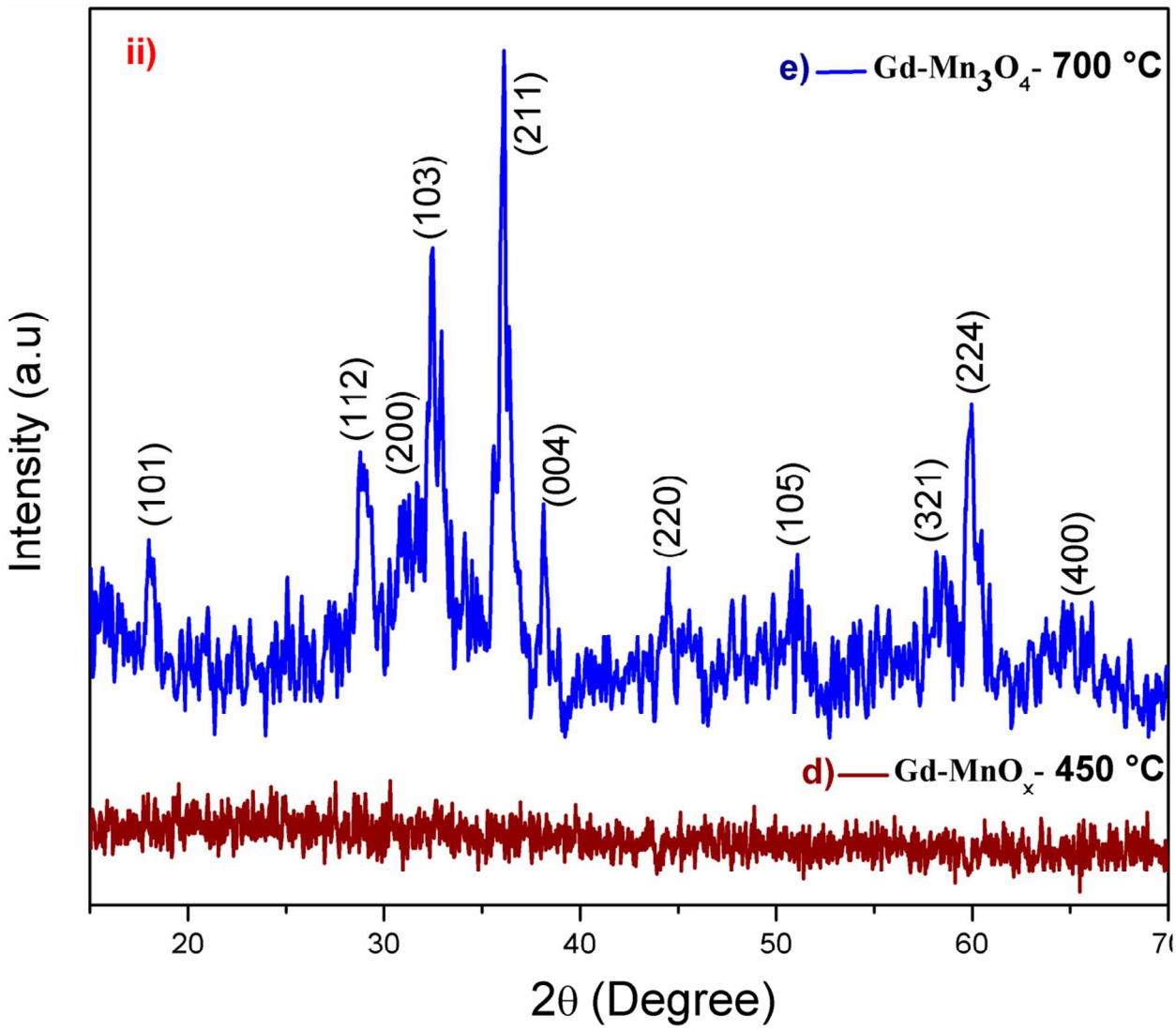

Fig. 1. XRD pattern of (i) manganese oxalate a) as synthesized, calcined at b) 450°C, c) 700 °C, (ii). Gd-doped manganese oxalate samples calcined at d) 450, and e) 700 °C.

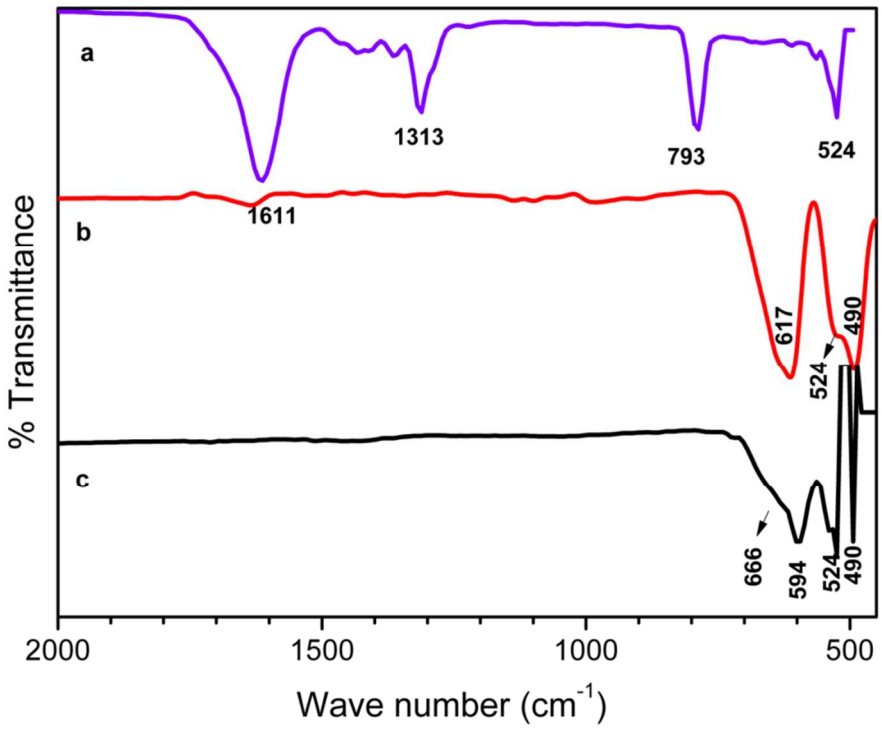

Fig. 2. FT-IR spectra of (a) manganese oxalate, (b) manganese oxide calcined at 700 °C, and (c) Gd-doped manganese oxide calcined at 700 °C.

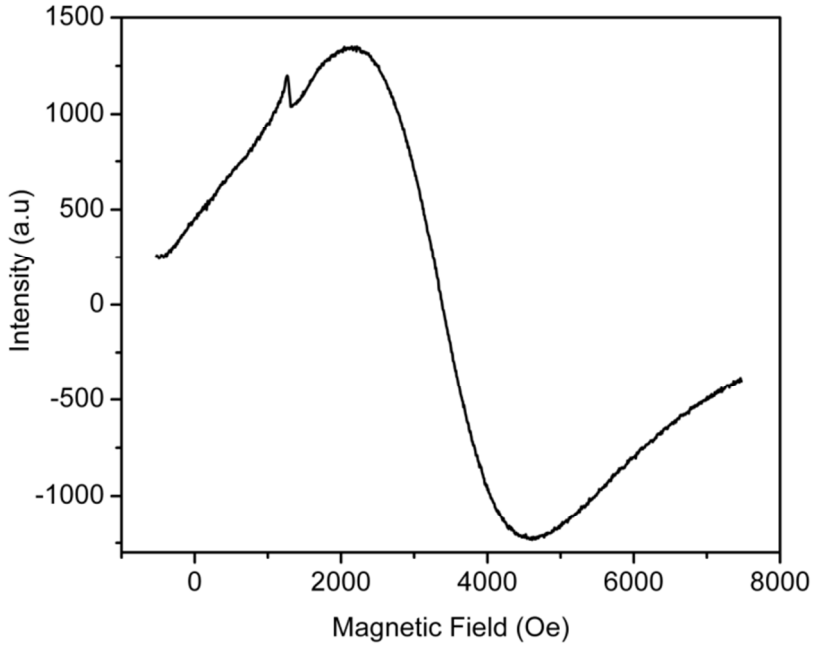

Fig. 3.EPR spectrum of Gd-Mn_3O_4.

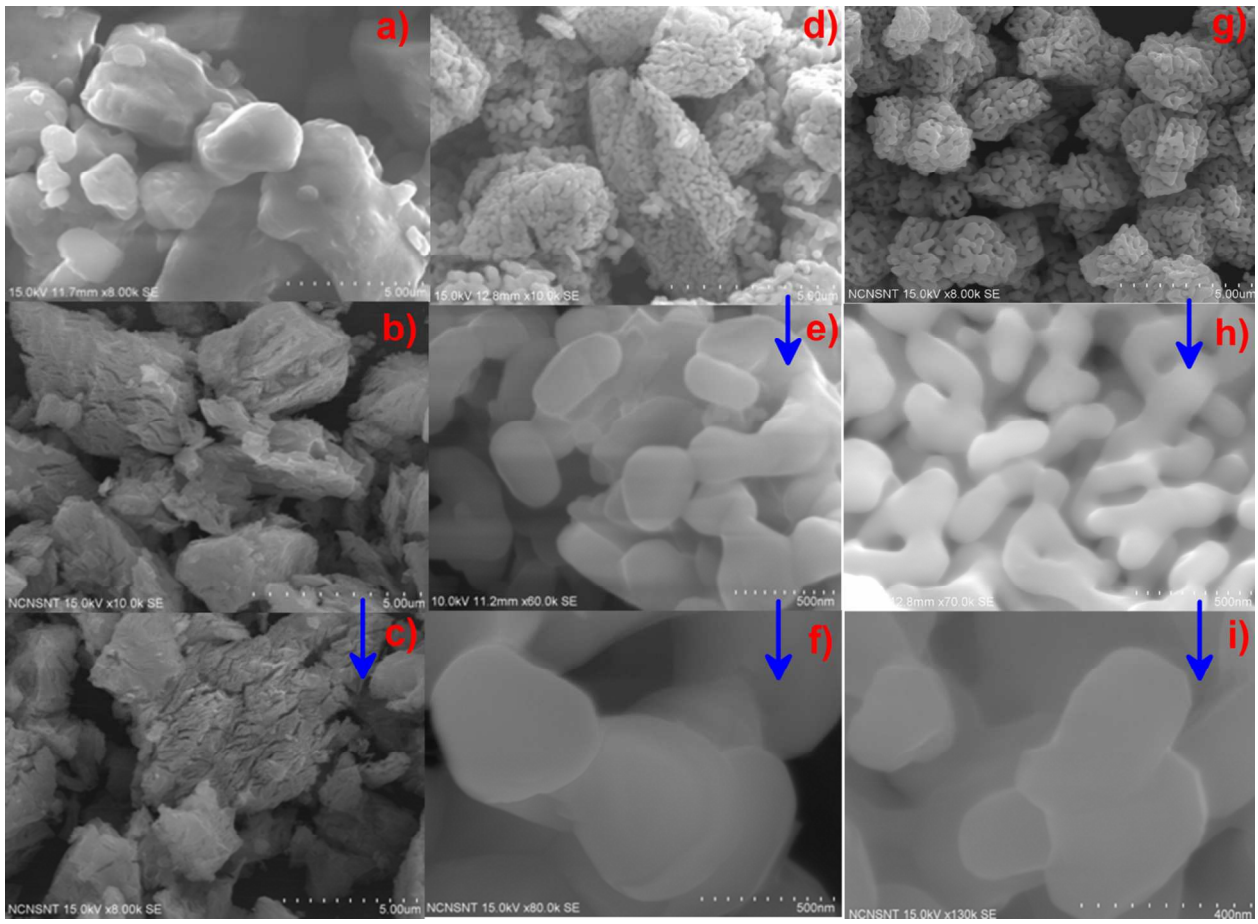

Fig. 4 FESEM images of MnC_2O_4 (a) as synthesized, calcined at (b, c) 450, (d, e, f) 700, and (g, h, i) 900 °C (magnified views are indicated with blue arrow line).

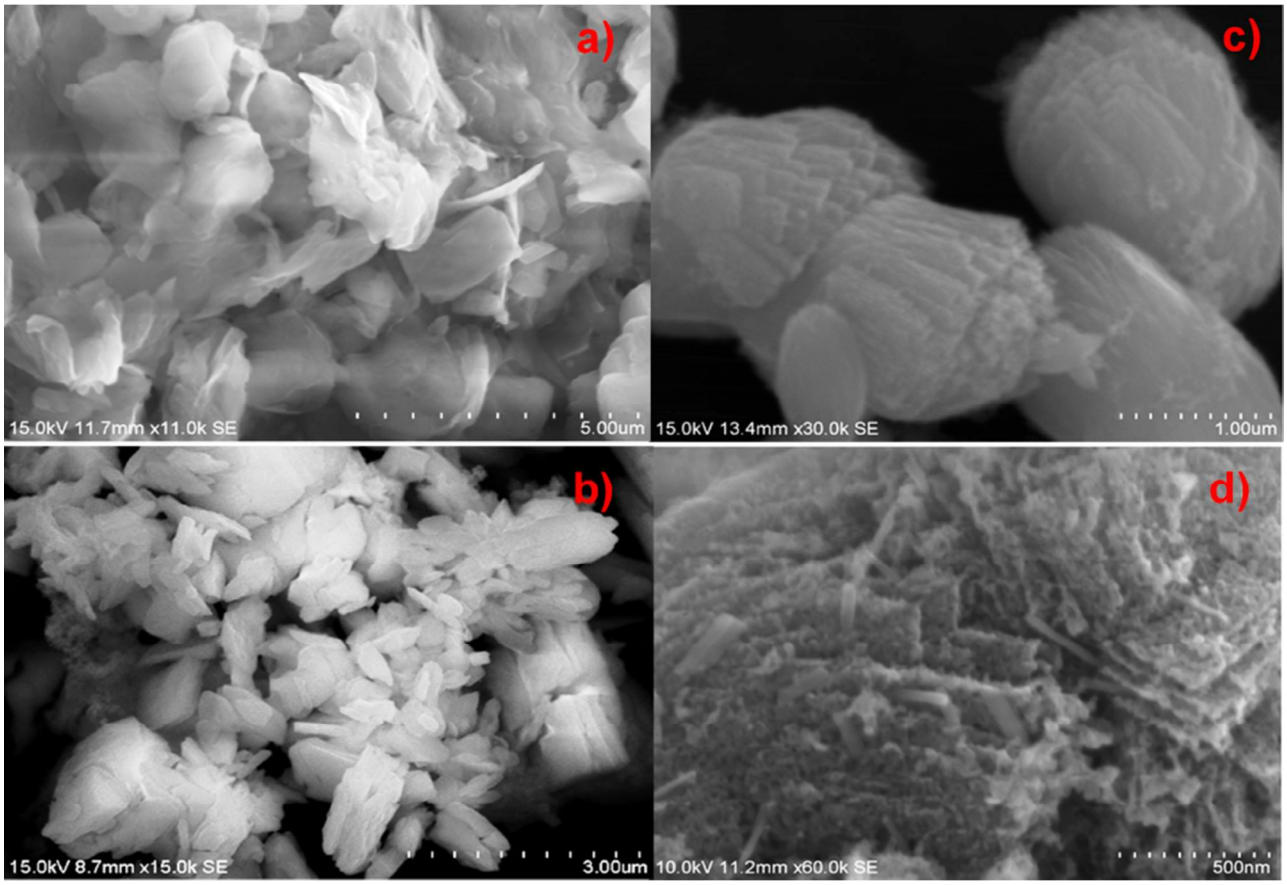

.

Fig. 5. FESEM images of Gd doped MnC_2O_4 (a) as synthesized, calcined at (b) 450, (c) 450 (magnified image) and (d) 700 °C.

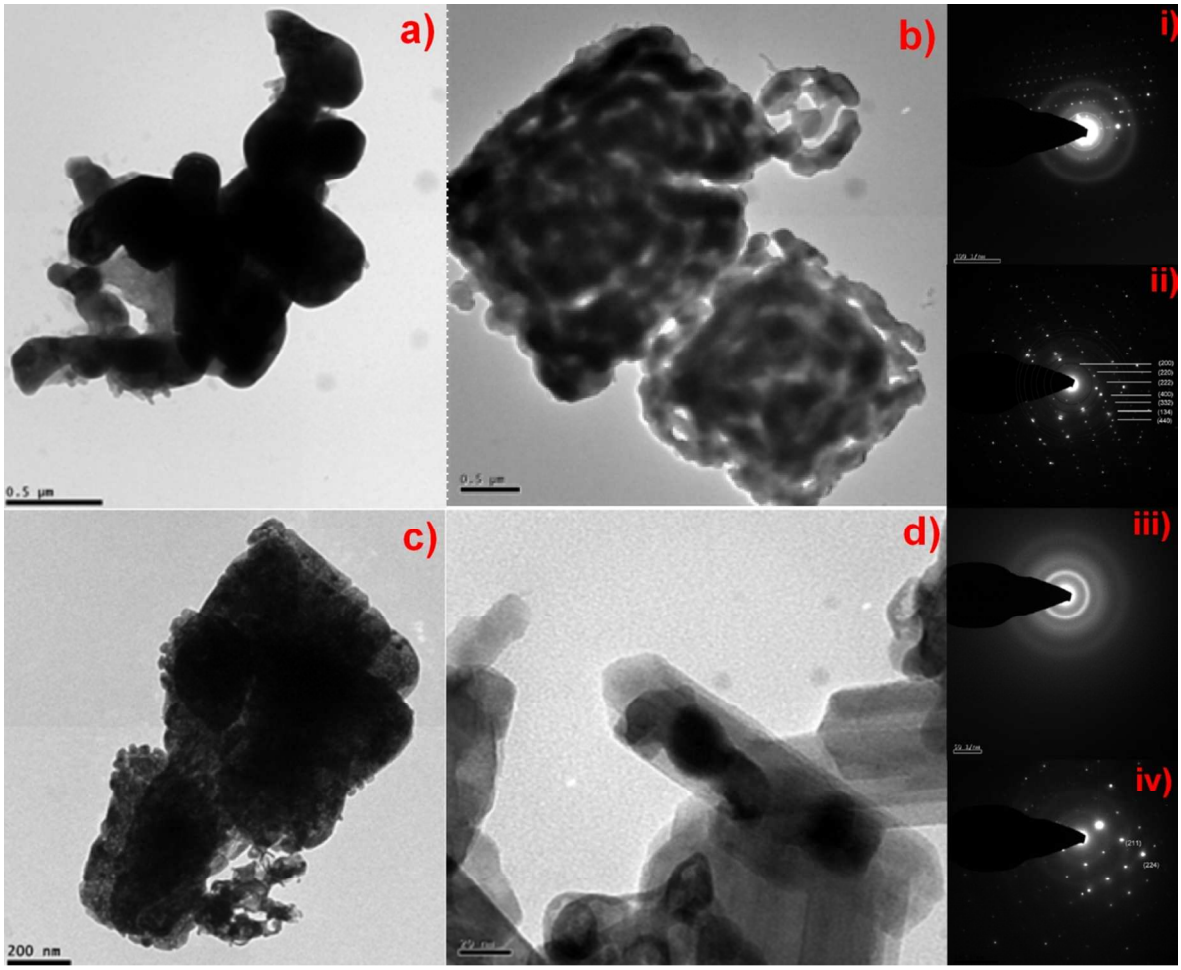

Fig. 6. HRTEM images of MnC_2O_4 calcined at (a) 450, (b) 700 °C, Gd doped MnC_2O_4 calcined at (c) 450, (d) 700 °C, and (i, ii, iii, iv) SAED patterns, respectively.

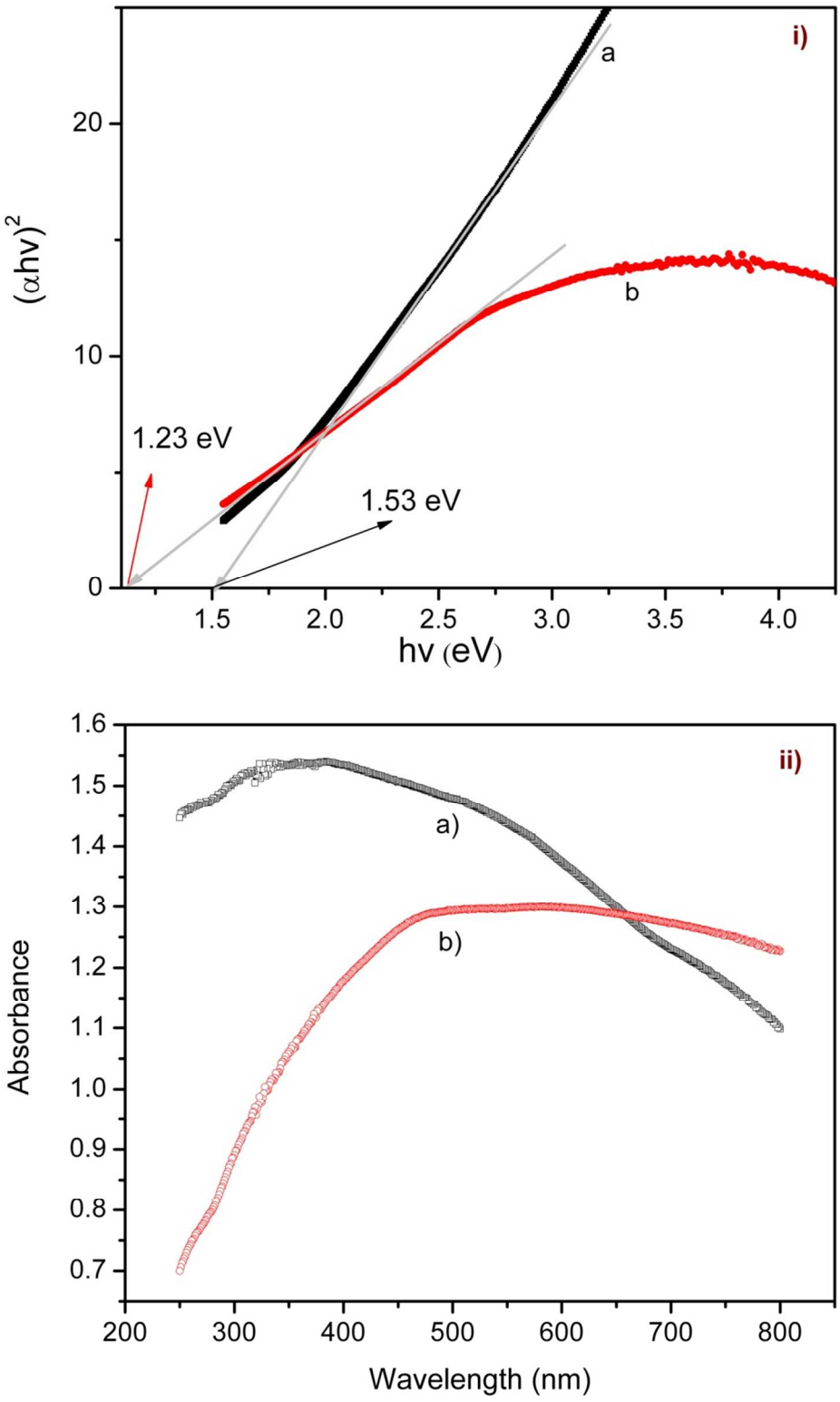

Fig. 7 (i). Tauc plot and (ii). DRS-UV-Vis absorption spectra of (a) Gd-doped manganese oxide, and (b) manganese oxide, calcined at 700 °C, respectively.

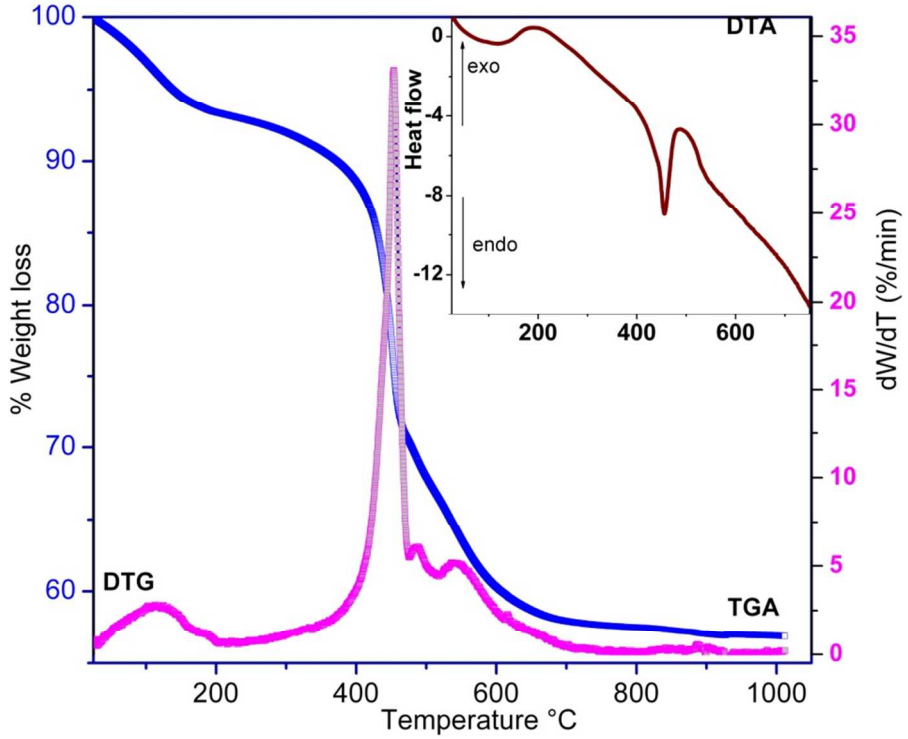

Fig. 8. TG-DTA-DTG of Gd-MnC_2O_4.

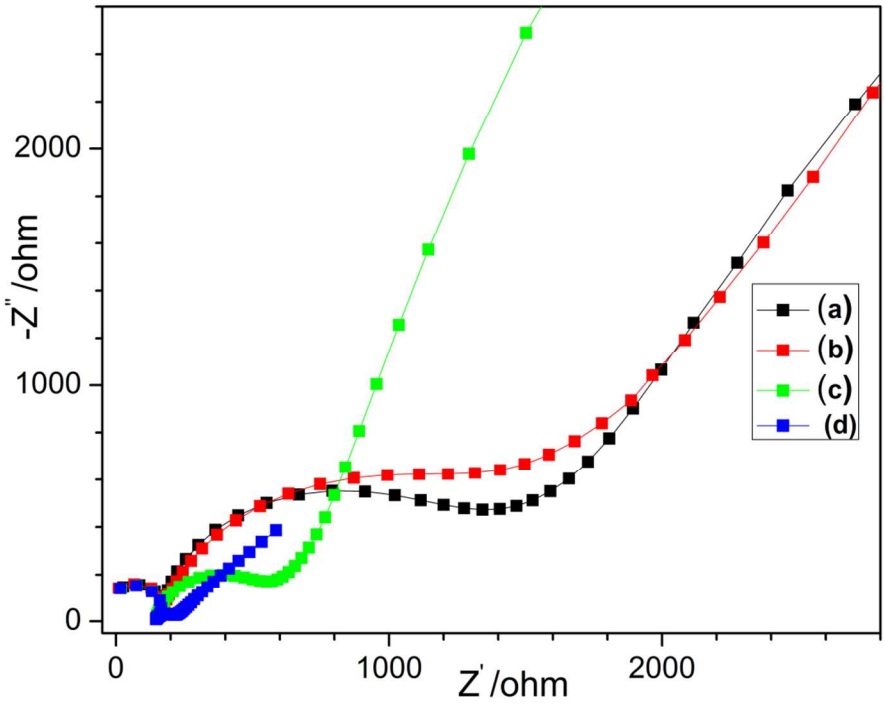

Fig. 9. Typical Nyquist impedance spectra of a) Gd-doped manganese oxide 700 °C, b) Gd-doped manganese oxide at 450 °C, c) manganese oxide and d) bare GCE.

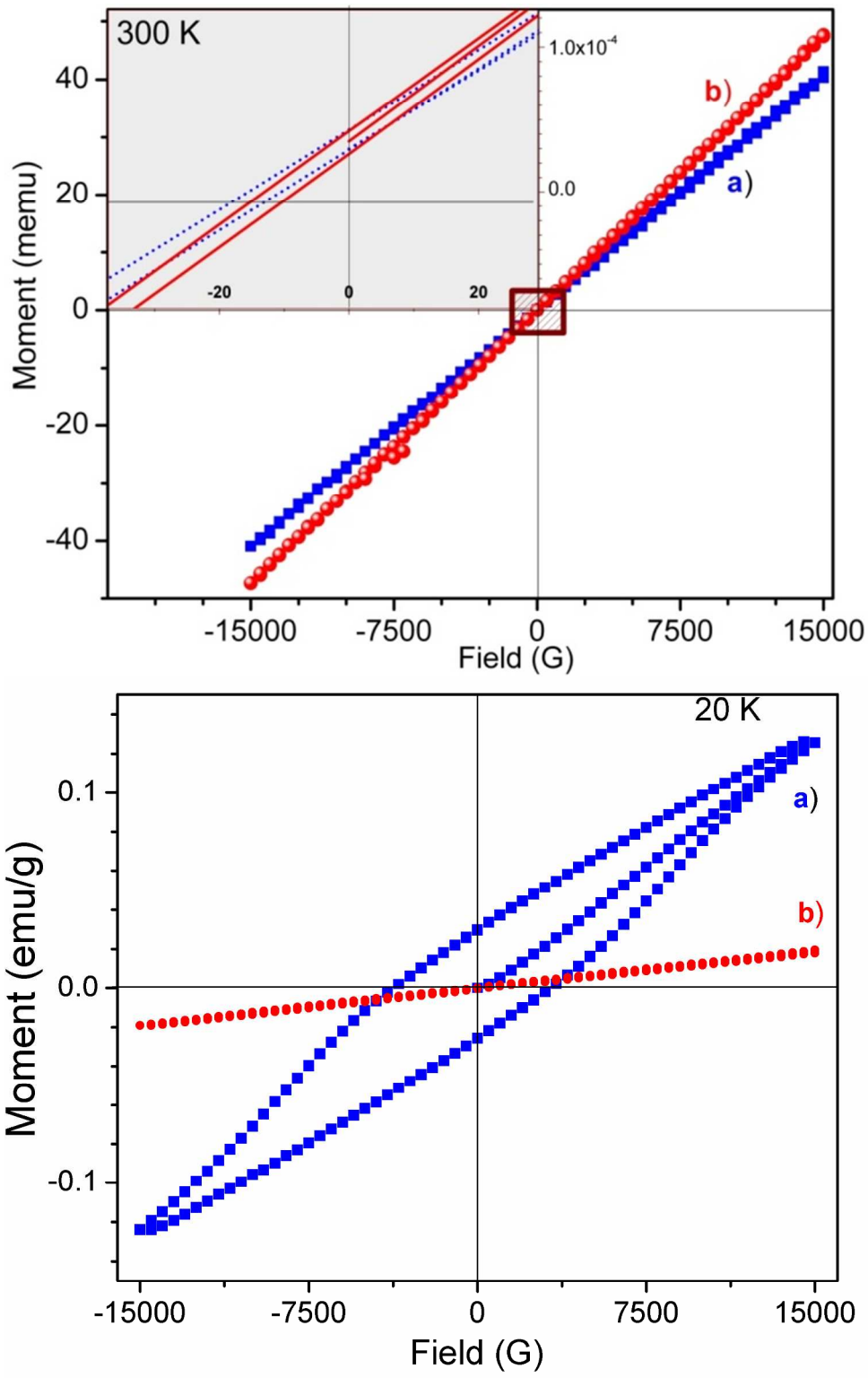

Fig. 10. VSM measurements carried out at 300 K, and 20 K for samples calcined at 700 °C

(a) Gd-doped manganese oxide, and (b) manganese oxide.

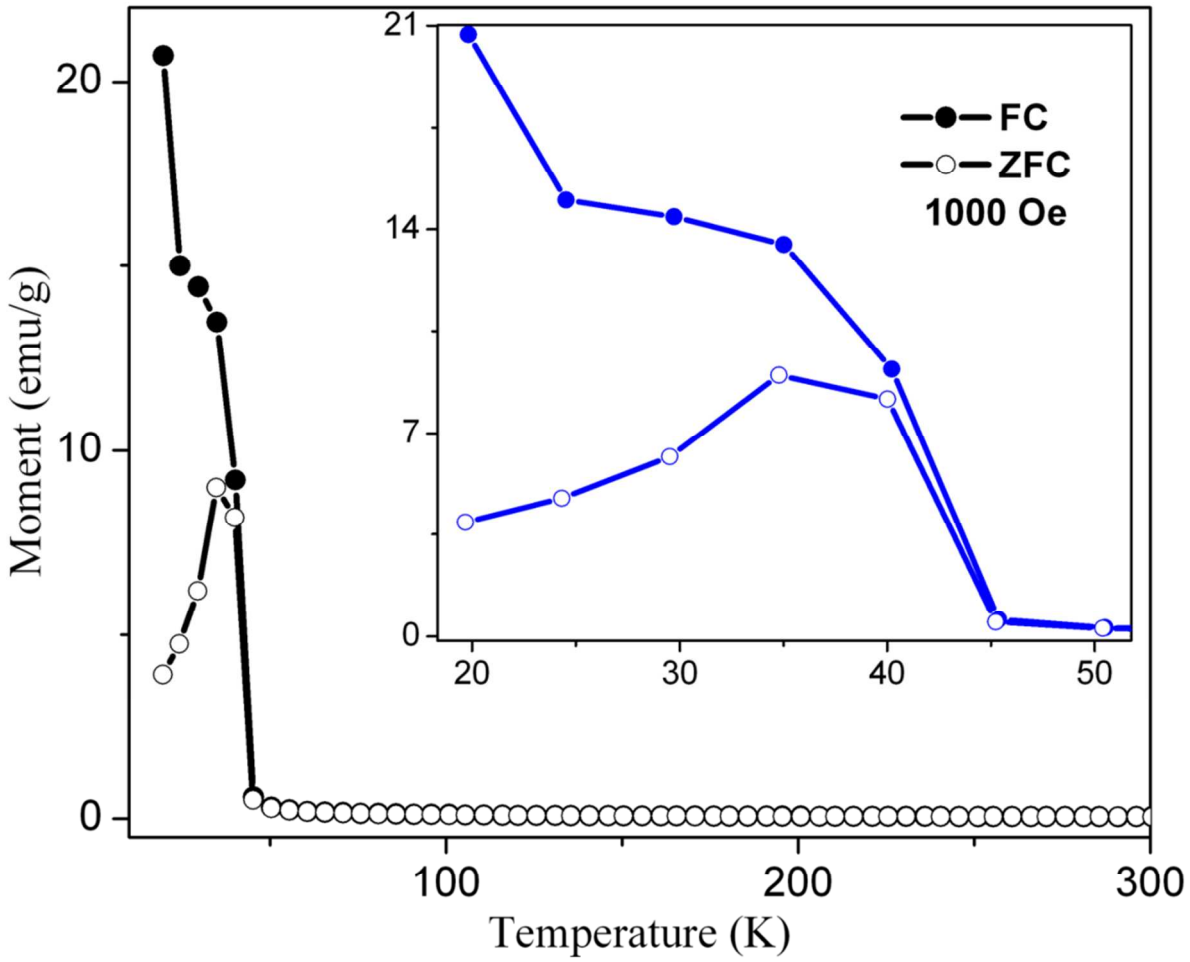

Fig.11. FC and ZFC magnetization cureves of Gd-doped manganese oxide as a function of temperature under an applied field of 1000 Oe .

Reference:

1. Y. Tan, L. Meng, Q. Peng and Y. Li, *Chem. Commun*., 2011, **47**, 1172-1174.
2. J. Hou, Y. Li, M. Mao, L. Ren, and X. Zhao, *ACS Appl. Mater. Interfaces*, 2014, **6**, 14981-14987
3. Y. Moritomo, A. Asamitsu, H. Kuwahara and Y. Tokura, *Nature*, 1996, **380**, 141-144.
4. J. Gao, H. Gu, and B. Xu, *Acc. Chem. Res*. 2009, **42**, 1097-1107
5. H. Wang, L.F. Cui, Y. Yang, H. Sanchez Casalongue, J. T. Robinson, Y. Liang, Y. Cui and H. Dai, *J. Am. Chem. Soc*., 2010, **132,** 13978-13980.
6. R. Suresh, K. Giribabu, R. Manigandan, A. Stephen, and V. Narayanan, *RSC Adv.*, 2014, **4**, 17146–17155.
7. Y.G. Wang, L. Cheng, F.Li, H.M. Xiong, and Y.Y. Xia, *Chem. Mater.,* 2007, **19,** 2095-2101.
8. D. Wang, Y. Li, Q. Wang and T. Wang, *Eur. J. Inorg. Chem.,* 2012, **2012,** 628-635.
9. A. Giri, N. Goswami, M. Pal, M. T. Z. Myint, S. Al-Harthi, A. Singha, B. Ghosh, J. Dutta and S. K. Pal, *J. Mater. Chem. C,* 2013, **1,** 1885-1895.
10. S. K. Bikkarolla, F. Yu, W. Zhou, P. Joseph, P. Cumpson and P. Papakonstantinou, *J. Mater. Chem. A,* 2014, **2**, 14493-14501.
11. S.L. Suib, *Acc. Chem. Res.,* 2008, **41**, 479-487.
12. J.M. Shin, R.M. Anisur, M.K. Ko, G.H. Im, J.H. Lee and I.S. Lee, *Angew. Chem., Int. Ed.,* 2009, **48**, 321-324.
13. A.N. Chowdhury, M.S. Azam, M. Aktaruzzaman, and A. Rahim, *J. Hazard. Mater.,* 2009, **172**, 1229-1235.
14. J.H. Park, I. Jang, B. Kwon, S.C. Jang, and S.G. Oh, *Mater. Res. Bull.*, 2013, **48**, 469-475
15. X. Yu, J. He, D. Wang, Y. Hu, H. Tian, and Z. He, *J. Phys. Chem. C,* 2012, **116**, 851-860.
16. X.G. Lei, S. Jockusch, N.J. Turro, D.A. Tomalia, and M.F. Ottaviani, *J. Colloid Interface Sci.,* 2008, **322,** 457-464.
17. R. Manigandan, K. Giribabu, R. Suresh, L. Vijayalakshmi, A. Stephen, and V. Narayanan, *Mater. Res. Bull.*, 2013, **48**, 4210-4215.
18. W.B.S. Machini, C.S. Martin, M.T. Martinez, S.R. Teixeira, H.M. Gomes, and M.F.S. Teixeira, *Sens. Actuator B Chem.,* 2013, **181**, 674-680

19. R. Manigandan, K. Giribabu, R. Suresh, S. Munusamy, S. Praveen kumar, S. Muthamizh, T. Dhanasekaran, A. Padmanaban, and V. Narayanan, *RSC Adv*., 2015, **5**, 7515-7521.
20. N. Dhananjaya, H. Nagabhushana, B.M. Nagabhushana, B. Rudraswamy, C. Shivakumara, P. Ramesh, and R.P.S. Chakradhar, *Physica B*, 2011, **406**, 1645-1652.
21. G. Muralidharan, N. Bhat and V. Santhanam, *Nanoscale,* 2011, **3,** 4575-4579.
22. J.C. Wang, C.T. Lin, P.C. Chou, and C.S. Lai, *Microelectron. Reliab.,* 2012, **52**, 635-641.
23. S.S. Liu, S. Gao, J. W. Zillera and W. J. Evans, *Dalton Trans.,* 2014, **43**, 15526-15531.
24. D. Kim, J. Hong, Y. R. Park and K. J. Kim, J. *Phys.: Condens. Matter,* 2009, **21**, 195405-195408.
25. R.-A. Eichel, *Phys. Chem. Chem. Phys*., 2011, **13**, 368–384
26. O.Y. Gorbenko, I.E. Graboy, V.A. Amelichev, A.A. Bosak, A.R. Kaul, B. Güttler, V.L. Svetchnikov, and H.W. Zandbergen, *Solid State Commun*., 2002, **124**, 15-20.
27. Z. Chen, C. Wang, H. Zhou, L. Sang and X. Li, *CrystEngComm.,* 2010, **12**, 845-852.
28. L. Zhang, L. Zhao and J. Lian, *RSC Adv.,* 2014, **4**, 41838-41847.
29. J. Du, Y. Gao, L. Chai, G. Zou, Y. Li, and Y. Qian, *Nanotechnology*, 2006, **17**, 4923-4928.
30. S. Sambasivam, G.J. Li, J.H. Jeong, B.C. Choi, K.T. Lim, S.S. Kim, and T.K. Song, *J. Nanopart. Res.,* 2012, **14**, 1138-1147.
31. W.S. Kijlstra, E.K. Poels, A. Bliek, B.M. Weckhuysen, and R.A. Schoonheydt, *J. Phys. Chem. B*, 1997, **101**, 309-316.
32. A.M. Smith and S. Nie, *Acc. Chem. Res*., 2010, **43**, 190-200.
33. C.C. Yu, L.X. Zhang, J.L. Shi, J.J. Zhao, J.H. Gao, and D.S. Yan, *Adv. Funct. Mater.,* 2008, **18**, 1544-1554.
34. S. Sobhani and Z. Pakdin-Parizi, *RSC Adv*., 2014, **4**, 13071-13077.
35. U. P. N. Tran, K. K. A. Le and N. T. S. Phan, *ACS Catalysis*, 2011, **1**, 120-127.
36. K. Dhanapal, T.A. Revathy, M.A. Raj, V. Narayanan, and A. Stephen, *Appl. Surf. Sci.,* 2014, **313**, 698-703.
37. B. Klingenberg and M.A. Vannice, *Chem. Mater*., 1996, **8**, 2755-2768.
38. P. Z. Si, D. Li, C. J. Choi, Y. B. Li, D. Y. Geng, and Z. D. Zhang, *Solid State Commun*., 2007, **142**, 723-726.